ACS NANO
Cite This: ACS Nano 2017, 11, 10583-10590
www.acsnano.org

ARTICLE

Noninvasive Cathodoluminescence-Activated Nanoimaging of Dynamic Processes in Liquids

Connor G. Bischak,[†,‡] Rebecca B. Wai,[†] Charles Cherqui,[§] Jacob A. Busche,[§] Steven C. Quillin,[§] Craig L. Hetherington,[†,‡] Zhe Wang,[∥] Clarice D. Aiello,[†,¶] Darrell G. Schlom,[⊥,#] Shaul Aloni,[⊗,▽] D. Frank Ogletree,[⊗,▽] David J. Masiello,[§] and Naomi S. Ginsberg*[,†,‡,⊗,○,◆]

[†]Department of Chemistry and [◆]Department of Physics, University of California, Berkeley, California 94720, United States

[‡]Molecular Biophysics and Integrative Bioimaging Division, Lawrence Berkeley National Laboratory, Berkeley, California 94720, United States

[§]Department of Chemistry, University of Washington, Seattle, Washington 98195, United States

[∥]School of Applied and Engineering Physics and [⊥]Department of Materials Science and Engineering, Cornell University, Ithaca, New York 14853, United States

[#]Kavli Institute at Cornell for Nanoscale Science, Ithaca, New York 14853, United States

[⊗]Materials Science Division and [▽]Molecular Foundry, Lawrence Berkeley National Laboratory, Berkeley, California 94720, United States

[○]Kavli Energy NanoScience Institute, Berkeley, California 94720, United States

Supporting Information

ABSTRACT: ***In situ*** **electron microscopy provides remarkably high spatial resolution, yet electron beam irradiation often damages soft materials and perturbs dynamic processes, requiring samples to be very robust. Here, we instead noninvasively image the dynamics of metal and polymer nanoparticles in a liquid environment with subdiffraction resolution using cathodoluminescence-activated imaging by resonant energy transfer (CLAIRE). In CLAIRE, a free-standing scintillator film serves as a nanoscale optical excitation source when excited by a low energy, focused electron beam. We capture the nanoscale dynamics of these particles translating along and desorbing from the scintillator surface and demonstrate 50 ms frame acquisition and a range of imaging of at least 20 nm from the scintillator surface. Furthermore, in contrast with *in situ* electron microscopy, CLAIRE provides spectral selectivity instead of relying on scattering alone. We also demonstrate through quantitative modeling that the CLAIRE signal from metal nanoparticles is impacted by multiplasmonic mode interferences. Our findings demonstrate that CLAIRE is a promising, noninvasive approach for super-resolution imaging for soft and fluid materials with high spatial and temporal resolution.**

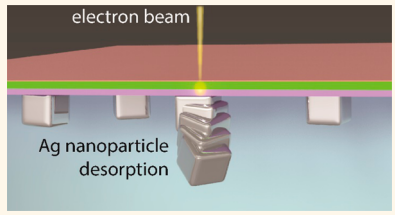

KEYWORDS: *nanoimaging, cathodoluminescence, super-resolution imaging, plasmonic enhancement*

Noninvasively observing dynamics in liquids at the nanoscale remains a significant challenge for elucidating processes occurring in both biological systems and soft functional materials. For instance, self-assembly processes in biology often occur at the nanoscale and are difficult to probe using traditional electron and optical microscopies.[1,2] In materials applications, advances in electron microscopy have enabled the visualization of dynamic processes, such as solution-phase nanoparticle motion, growth, and etching, with high spatial resolution and fast acquisition rates.[3−8] Although progress has been made to limit exposure, electron imaging in liquids can damage or chemically transform the sample or alter its dynamics.[7,8] Electron microscopy also lacks the spectrally selective excitation and detection capabilities of fluorescence microscopy, instead relying on contrast from electron scatter, which is typically too weak for soft materials imaging. Alternatively, far-field super-resolution fluorescence imaging methods, such as stimulated emission depletion (STED) microscopy and stochastic localization imaging techniques, are capable of noninvasively imaging with nanoscale spatial resolution and spectral selectivity.[9−13] These super-resolution microscopies, however, require fluorescent labels with specific photophysical properties, such as strong fluorescence, stimulated emission, or photoswitchability, and often lack the temporal resolution to capture dynamics on the characteristic time scales of many biological processes (see the Supporting Information).

Received: August 25, 2017
Accepted: September 26, 2017
Published: September 28, 2017

Downloaded via UNIV OF SAO PAULO on July 14, 2020 at 19:34:00 (UTC).
See https://pubs.acs.org/sharingguidelines for options on how to legitimately share published articles.

© 2017 American Chemical Society

DOI: 10.1021/acsnano.7b06081
ACS Nano 2017, 11, 10583−10590

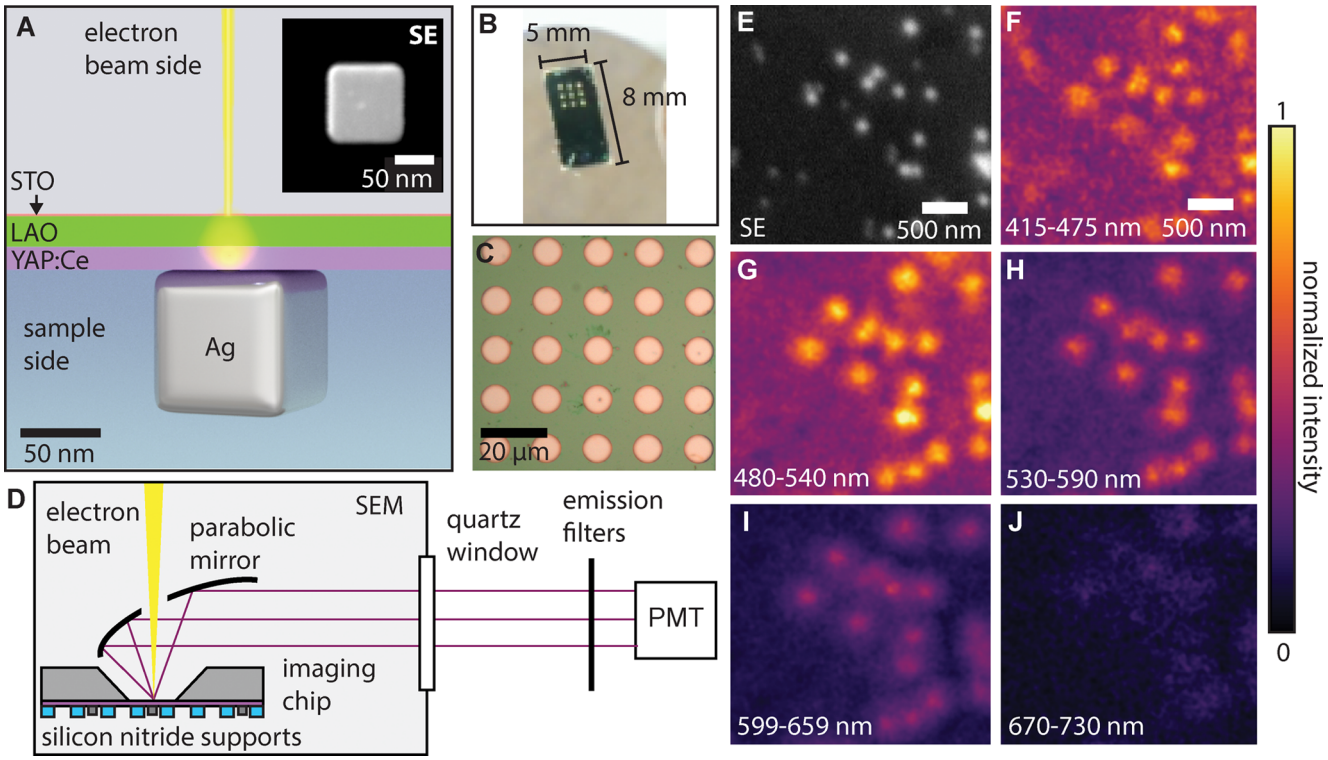

Figure 1. CLAIRE imaging of 100 nm Ag nanocubes using free-standing scintillator membranes. (A) Schematic of CLAIRE imaging of Ag nanocubes with a scanning electron microscopy (SEM) image of a 100 nm Ag nanocube in the inset. The free-standing scintillator film is composed of buffer layers of 20 nm thick $LaAlO_3$ (LAO) and 1.2 nm thick $SrTiO_3$ (STO) as well as the scintillator film, 15 nm thick $YAlO_3$:Ce (YAP:Ce). (B) Photograph of CLAIRE imaging device. (C) Reflected bright field image of circular free-standing scintillator film windows inside an etched silicon well of the fabricated chip. Free-standing YAP:Ce windows appear as pink circles surrounded by a supporting layer of silicon nitride. (D) Schematic of CL detection apparatus. (E) SEM image of Ag nanocubes through the free-standing scintillator film at 10 kV. (F–J) CLAIRE images of Ag nanocubes at 1.8 kV with different emission filters. In E–J, the image intensities are scaled so that the global maximum is set at 1 and the global minimum is at 0.

To leverage the noninvasiveness and spectral selectivity of fluorescence microscopy and the nanoscale resolution and fast acquisition speeds of electron microscopy, we developed cathodoluminescence (CL)-activated imaging by resonance energy transfer (CLAIRE) to image dynamics in liquids with high spatial and temporal resolution. In standard CL microscopy, an image is formed by collecting electron beam-generated light for each beam position as it scans across the sample. CL microscopy has been widely used to image robust luminescent samples and metal nanostructures.[14−21] In some cases, luminescent nanoparticle probes have been used for correlative CL and secondary electron (SE) imaging in biological samples,[22,23] yet electron beam-induced damage precludes imaging dynamics in soft materials. In CLAIRE, a focused, low energy electron beam excites a scintillator film, generating a nanoscale near-field optical excitation source. More specifically, electrons scatter within the scintillator, generating electronic excitations of luminescent dopants.[14] By using a low energy electron beam, electrons do not directly interact with the sample. Instead, excited scintillator dopants in the excitation volume can interact with the sample in the near field either by coupling to plasmons in metal nanoparticles through resonant dipole interactions[24−26] or by Förster resonance energy transfer (FRET) to a compatible chromophore. Although these two forms of coupling are most commonly used, any near-field interaction with the scintillator dopants can in principle alter the scintillator emission to generate image contrast, even if the sample itself is not luminescent. By scanning the electron beam and correlating either the scintillator or sample emission with the position of the beam, a nanoscale image of the underlying sample is formed without any direct interactions between the electron beam and the sample.

Previously, we fabricated scintillator films composed of cerium-doped yttrium aluminum perovskite ($YAlO_3$:Ce or YAP:Ce), which serve as a bright, robust, uniform excitation source for CLAIRE imaging when excited by a focused electron beam.[27] We also showed that CLAIRE can image both metal nanostructures through plasmonic enhancement of the Ce^{3+} dopants in the scintillator film and luminescent polymer blends through FRET with high spatial resolution.[28] In this previous implementation of CLAIRE, samples had to be encapsulated in a solid matrix to provide support for the very thin scintillator film. Here, we demonstrate imaging dynamics in liquid with CLAIRE by virtue of using a microfabricated CLAIRE imaging device whose key feature is a set of free-standing scintillator films only tens of nanometers thick. The free-standing scintillator films allow for easy deposition of the sample and enable CLAIRE imaging of samples in a liquid environment. Using Ag nanoparticles and luminescent polymer nanoparticles, we show that CLAIRE is capable of resolving nanoparticle desorption and translation along the scintillator surface. Together, these examples of dynamic nanoscale imaging establish CLAIRE as a promising super-resolution imaging platform capable of nanoscale imaging with high spatial and temporal resolution.

DOI: 10.1021/acsnano.7b06081
ACS Nano 2017, 11, 10583−10590

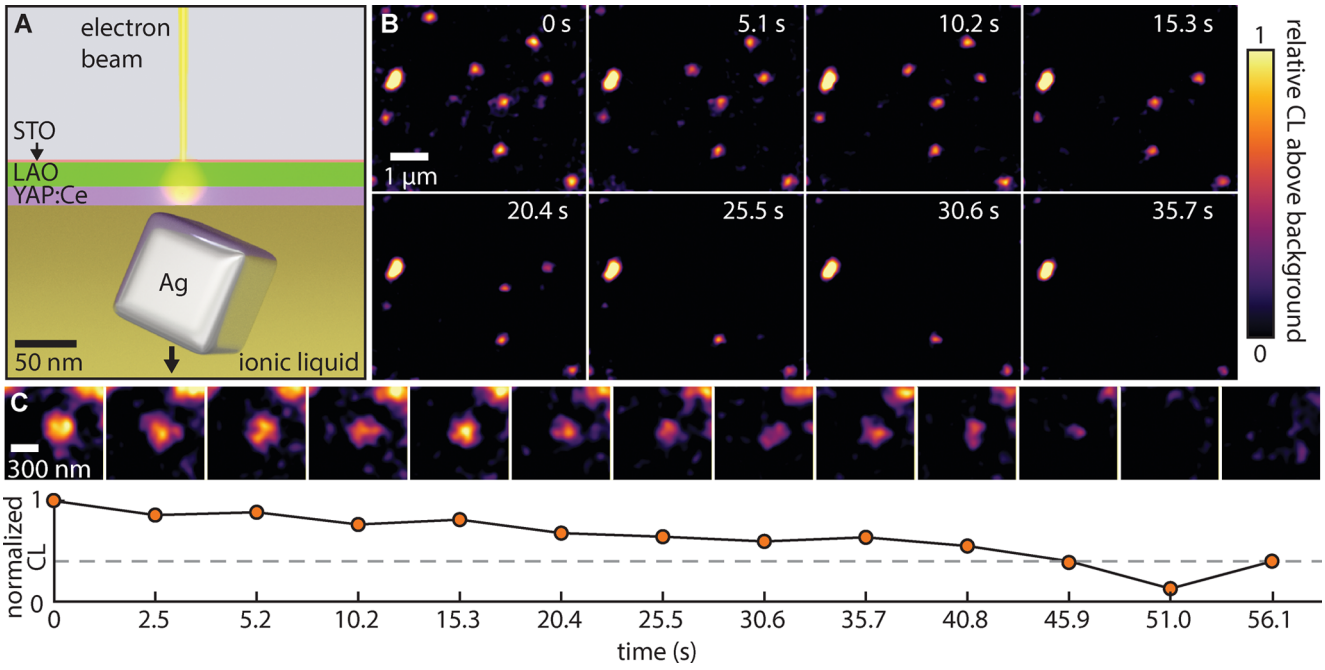

Figure 2. Imaging dynamic desorption of Ag nanocubes with CLAIRE microscopy. (A) Schematic of CLAIRE imaging of Ag nanocubes in ionic liquid. (B) CLAIRE imaging time series of Ag nanocube desorption. Images are collected every 2.6 s. (C) CLAIRE images of an Ag nanocube more gradually desorbing from the scintillator surface and the corresponding nanoparticle CLAIRE intensity as a function of time below. The dotted line is the average background CL intensity. In all CLAIRE images, the average background is subtracted, and then the frames all normalized by the global maximum.

RESULTS AND DISCUSSION

The major technical requirement for imaging in liquids with CLAIRE is a free-standing scintillator film. We developed a fabrication method to produce free-standing scintillator films that are mechanically stable without any substrate support. The free-standing scintillator film is composed of 15 nm-thick YAP:Ce on two buffer layers, $LaAlO_3$ (LAO) and $SrTiO_3$ (STO), as described in Figure S1. The buffer layers allow for lattice-matching between the silicon substrate and YAP:Ce scintillator film and are vital for growing epitaxial thin films of YAP:Ce.[27] As shown schematically in Figure 1a, the free-standing scintillator allows for the electron beam to excite the scintillator from one side, while the sample is positioned on the opposite side of the free-standing film. A photograph of the CLAIRE imaging device is shown in Figure 1b. Each of the nine etched wells in silicon in the CLAIRE imaging device contain an array of 50−100 circular YAP:Ce scintillator imaging windows that are ∼10 μm across and are supported by a silicon nitride grid with cylindrical wells (Figure 1c and Figure S2). For imaging, the sample is deposited on the scintillator within these silicon nitride wells, and the CLAIRE imaging device is placed in a scanning electron microscope (SEM) modified for CL detection (Figure 1d). Before using the free-standing scintillator films for CLAIRE, we determined that 1.8 kV is the optimal accelerating voltage to use for CLAIRE by detecting the electrons penetrating through the film at a range of accelerating voltages and then comparing our measurements to Monte Carlo simulations of electron-scattering trajectories within the film (Figure S3).

Prior to exploring the ability of CLAIRE to capture dynamics of particles in liquids, we characterized the CLAIRE signal from 100 nm Ag nanocubes deposited on the bottom surface of the scintillator film, as shown schematically in Figure 1a, with the inset showing a SE image of an Ag nanocube. An absorption spectrum of the Ag nanocubes is shown in Figure S4. To ensure that our signal is due to the presence of the nanocubes, we first captured an electron image by exciting them directly through the free-standing scintillator film at 10 kV (Figure 1e). We then reduced the electron beam accelerating voltage to 1.8 kV for CLAIRE imaging (Figure 1f−j). The CLAIRE images show that the presence of the Ag nanocubes locally enhances the scintillator optical emission above its background emission level, producing an image similar to the SE image in Figure 1e. By comparing the SE and CLAIRE images, we find that we can distinguish two Ag nanocubes that are separated by a gap of only ∼20 nm using CLAIRE (Figure S5). We also find that the imaging resolution is comparable in each of a series of spectral windows except for the 670−730 nm range because it has a low signal-to-noise ratio. We achieve the highest ratio between the Ag CLAIRE signal and scintillator background of 2.8 in the 480−540 nm spectral window presumably due to the wavelength-dependent plasmon response of the nanocubes (Figure S6). Therefore, we use the spectral detection range of 480−540 nm to achieve the highest possible CLAIRE signal while imaging Ag nanocube motion in liquid.

To demonstrate that CLAIRE is capable of imaging dynamic processes, we deposit the same type of 100 nm Ag nanocubes on the surface of the YAP:Ce film of the imaging chip and cover them with a droplet of low vapor pressure ionic liquid (1-butyl-3-methylimidazolium hexafluorophosphate, BMIM PF_6) before flipping the chip over for CLAIRE (Figure 2a). As we repeatedly raster the electron beam across the scintillator, we see bright spots corresponding to the Ag nanocubes disappear, presumably due to the desorption of the Ag nanocubes from the scintillator surface (Figure 2b, Figure S7, video S1, and video S2). By tracking the intensity of each particle over a time series of frames, we observe that most nanocubes disappear abruptly within a few seconds, yet a small number desorb more

DOI: 10.1021/acsnano.7b06081
ACS Nano 2017, 11, 10583−10590

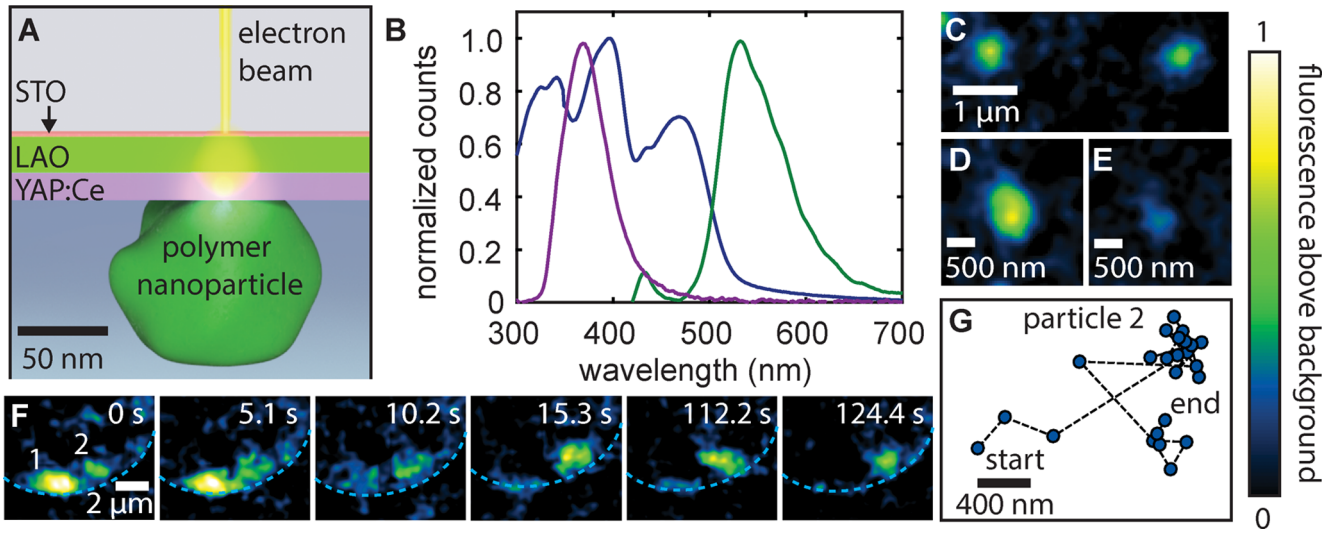

Figure 3. CLAIRE imaging of luminescent polymer nanoparticles. (A) Schematic of CLAIRE imaging PFO-F8BT nanoparticles. (B) CL spectrum of YAP:Ce (purple) with absorption (blue) and emission (green) spectra of F8BT/PFO nanoparticles. (C) CLAIRE image of polymer nanoparticles. (D) CLAIRE image of a PFO/F8BT nanoparticle. (E) Reduction of the emitted light in a CLAIRE image of the same nanoparticle as in D after bleaching at 10 kV. (F) Frames from a CLAIRE movie showing the dynamics of two polymer nanoparticles in an ionic liquid. The CLAIRE intensity of particle 1 decreases sharply with time, and particle 2 translates along the YAP:Ce surface. The blue dotted line is the edge of a YAP:Ce imaging window. (G) Centroid of particle 2 from each frame collected for the movie in (F) demonstrating particle translation and dwelling. In all CLAIRE images, the average background value is subtracted and the fluorescence signal is then normalized.

gradually (Figure S8). The slow desorption is presumably because they initially interact with the scintillator surface over multiple contact points whose number gradually diminishes during imaging. An example of a slowly desorbing nanocube along with a graph of the nanocube intensity during desorption is shown in Figure 2c. The CLAIRE images shown in Figure 2 are cropped from a larger 512 × 512 pixel 15 × 15 μm image acquired at 10 μs/pixel. Therefore, the acquisition time for the set of cropped images shown in Figure 2b was 1.23 s/frame with 1.43 s between frames, while for Figure 2c the acquisition time was 0.05 s/frame with 2.51 s between frames. There need not, however, be any pauses between frames. Here, the pauses are a result of zooming in on a region of interest smaller than the full frame size. The high temporal resolution of this image series demonstrates that CLAIRE can rapidly image dynamics at the nanoscale. Resolving the nanocube desorption represents a promising example of imaging a dynamic process with CLAIRE and unequivocally demonstrates that CLAIRE can capture dynamic processes with high spatial and temporal resolution. It would require further investigation to determine whether Ag nanocube desorption might be caused by electron beam-induced charging of the scintillator film, but because the scintillator film intercepts the electron beam, this approach is substantially less invasive than direct electron beam exposure.

Similarly, we show that CLAIRE can image more delicate luminescent polymer nanoparticles (Figure 3a). We chose nanoparticles composed of a blend of poly(9,9-di-*n*-octylfluorenyl-2,7-diyl) (PFO) and poly[((9,9-di-*n*-octylfluorenyl-2,7-diyl)-*alt*-co-(1,4-benzo-{2,1′,3}-thiadiazole)] (F8BT) because the CL emission spectrum of the YAP:Ce scintillator overlaps with the PFO/F8BT absorption spectrum for good FRET efficiency, and the red-shifted emission is easily detected with a 530−590 nm emission filter (Figure 3b). A CLAIRE image of two PFO/F8BT nanoparticles are shown in Figure 3c. The PFO/F8BT particles appear as bright spots in the CLAIRE image with a signal-to-background ratio of 3.5. The spots in the CLAIRE images are often not circular in shape, which could stem from irregularities in the shape or surface of the particle. By taking a line cut over the edge of a polymer particle and fitting with a sigmoidal function, we estimate that our resolution based on the 80/20 width of the sigmoidal fit is 88 nm (Figure S9), although three-dimensional irregularities in the particle shape or its configuration relative to the scintillator surface could affect the resolution measurement. To confirm the noninvasiveness of CLAIRE and that our contrast mechanism is FRET-based, we imaged a nanoparticle with CLAIRE at 1.8 kV (Figure 3d), bleached the particle through the scintillator at 10 kV for several seconds, and then reimaged the bleached particle at 1.8 kV (Figure 3e). As anticipated, we see a reduction in the CLAIRE emission from the particle after bleaching. Using FRET, we then image polymer particle motion while surrounding them in a low vapor pressure hydrocarbon oil. Figure 3f displays a series of frames showing nanoparticle dynamics, with the complete series of frames shown in Figure S10. Particle 1 sharply decreases in brightness after 10 s, presumably because it detaches from the scintillator surface (Figure S10). Particle 2 translates along the scintillator surface. By plotting the centroid position of particle 2 overlaid for all frames (Figure 3g), we observe particle translation and transient dwelling at different positions on the scintillator surface. We confirm that the imaging mechanism is noninvasive because the particle remains bright for the multiple minutes over which the movie is acquired instead of being bleached by the electron beam. Therefore, our example of observing polymer nanoparticle translation across the scintillator demonstrates the capability of CLAIRE to noninvasively image the evolution of soft materials in a liquid environment.

In addition to resolving nanoparticle motions in liquids, we evaluate the axial range of CLAIRE. When using plasmonic enhancement of the scintillator emission as a contrast mechanism, this range should roughly scale with the metal particle radius of curvature enabling imaging beyond a typical

DOI: 10.1021/acsnano.7b06081
ACS Nano 2017, 11, 10583−10590

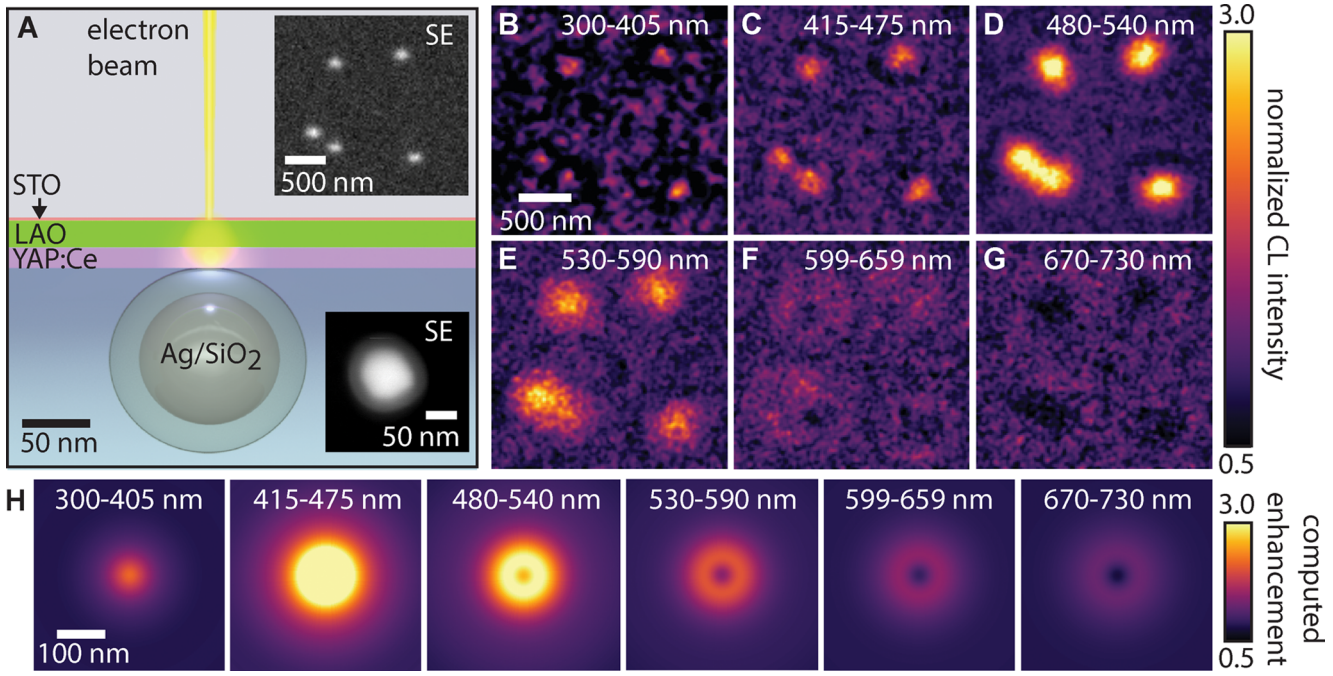

Figure 4. CLAIRE imaging and simulated CLAIRE images of 100 nm Ag particles with a 20 nm SiO_2 shell. (A) Schematic of CLAIRE imaging of 100 nm Ag particles with a 20 nm SiO_2 shell with SEM image of the Ag/SiO_2 core−shell particles through the free-standing YAP:Ce film at 10 kV in the upper inset and SEM image of the Ag/SiO_2 core−shell particles in the lower inset. (B−G) CLAIRE images of the Ag/SiO_2 core−shell nanoparticles acquired with different emission filters. The images are normalized with respect to the background, which is set at 1, and the maximum of all six images. (H) Simulated CLAIRE images of Ag/SiO_2 core−shell nanoparticles at different emission wavelengths.

FRET radius of ∼10 nm. As a test of CLAIRE's axial imaging range under these conditions, we image 100 nm Ag particles coated with 20 nm SiO_2 on the free-standing scintillator film in vacuum, as shown schematically in Figure 4a. The upper inset of Figure 4a shows an SE image of the Ag/SiO_2 nanoparticles through the scintillator film at 10 kV, while the bottom inset shows a direct SE image of the Ag/SiO_2 nanoparticles. We collect CLAIRE images of the Ag/SiO_2 core−shell particles in different wavelength ranges to determine the optimal wavelength range for imaging (Figure 4b−g). Even with the 20 nm SiO_2 spacer between the Ag particle and the scintillator film, we obtain CLAIRE images with a high signal-to-background ratio in the 480−540 nm spectral window. Although the resolution is <100 nm at and below the wavelengths that generate the strongest signal (Figure 4b−e), the best resolution of ∼<50 nm is obtained in the 300−405 nm spectral window (Figure S11). The signal strength is above the scintillator background at 300−405, 415−475, 480−540, and 530−590 nm. In the 599−659 nm spectral window, the CLAIRE signal appears as a bright halo surrounding a circle with suppressed intensity. At 670−730 nm, the CLAIRE signal of the nanoparticles is mostly lower than the scintillator background level. We observe a similar trend with 50 nm Ag particles coated in 20 nm SiO_2 (Figure S12).

We find that the spectrally dependent patterns in the CLAIRE images stem from the spatially and spectrally dependent enhancement of the Ce^{3+} dopants' radiative emission when they are in the vicinity of the nanoparticles. By computing the total power radiated by plasmon-enhanced dipole emitters oriented in the plane of the scintillator near a Ag-SiO_2 core−shell nanoparticle as well as by the dipole-induced plasmons of the nanoparticle, we produce simulated CLAIRE images (Figure 4h and Figure S13) that show the same spectral trend shown in Figure 4b−g and Figure S11. A direct comparison of the experimental and simulated CLAIRE images is given in Figure S14 and the Supporting Information. Since the Ce^{3+} dopants are a near-field excitation source for the plasmons, they interact with many of the nanoparticle's multipolar plasmon modes as dictated by the spectral and spatial dependence of the plasmon-dipole selection rules (see the Experimental Methods). This, combined with the well-known quenching effects in plasmon-enhanced fluorescence,[29] explains the spatial and spectral variations observed in Figure 4b−g and Figure S11. The same model generates a similar trend for 50 nm Ag nanoparticles coated with 20 nm SiO_2 (Figure S15) in agreement with CLAIRE (Figure S12). In contrast, 100 nm Ag nanocubes are expected to result in CLAIRE signals above the background across a wider spectral window because the interaction between the nanocube and the dielectric substrate leads to the presence of a more complicated set of plasmon modes for the Ce^{3+} dopants to interact with. This is in good agreement with the CLAIRE images in Figure 1f−j. Imaging of the core−shell Ag/SiO_2 particles with CLAIRE demonstrates that we can not only visualize particles at least 20 nm away from the surface of the scintillator film but also map the spatial profile of nanoparticle−substrate resonance energy transfer and determine which specific plasmons interact with which specific Ce^{3+} dopants. These calculations also suggest that CLAIRE can capture the dynamics of bare Ag particles even if they are not in contact with the scintillator surface.

CONCLUSIONS

By imaging both Ag and polymer nanoparticle motions in liquid environments, we have established CLAIRE as an imaging platform capable of capturing dynamics in liquids with high temporal and spatial resolution. The development of

DOI: 10.1021/acsnano.7b06081
ACS Nano 2017, 11, 10583−10590

intact free-standing scintillator films has been the key to enabling CLAIRE imaging in liquids. To image liquid samples using the free-standing scintillator films, CLAIRE leverages the high-resolution imaging capability of a focused electron beam, yet avoids direct interactions between the electron beam and the sample that are common in *in situ* electron microscopy. Using CLAIRE, we have demonstrated signal-to-background ratios greater than 3, resolution of features only 20 nm apart, and frame capture as fast as 50 ms. This noninvasive approach also takes advantage of spectrally selective excitation and emission, rather than electron scattering, to provide spectrally specific contrast—even in soft materials that would typically scatter too weakly in electron-based imaging. The absence of direct interactions between the electron beam and the sample in CLAIRE extends *in situ* nanoscale imaging to a much broader class of soft materials that are typically incompatible with electron imaging, leading to a more detailed observation of motion, assembly, and organization of delicate samples at nanometer length scales.

By further integrating the CLAIRE imaging chip into an encapsulated liquid cell, we envision expanding the capabilities of CLAIRE to imaging physiological biological samples and functional nanomaterials in an aqueous environment. The demonstrated axial range of CLAIRE using plasmonic nanoparticles is also promising for capturing dynamics that occur beyond the FRET radius of the scintillator film, as would be the case for capturing the motion of protein complexes on a supported lipid bilayer with metal nanoparticle labels. We also foresee imaging the evolution of other samples with endogenous fluorescence, such as protein complex reorganization in photosynthetic membranes, optoelectronic instabilities in optoelectronic materials, or the elusive electric double-layer configurations of electrolyte at a battery electrode's surface. CLAIRE imaging will provide the opportunity to combine the most redeeming features of state-of-the-art electron and super-resolution optical microscopies into a single platform that minimally influences complex systems as it resolves their evolution.

EXPERIMENTAL METHODS

Fabrication of CLAIRE Imaging Chips with Free-Standing YAP:Ce Scintillator Films. The growth and characterization of epitaxial YAP:Ce films are described in a prior publication.[27] Briefly, films of YAP:Ce (15−20 nm thick) were grown via pulsed laser deposition (PLD) onto silicon substrates (Virginia Semiconductor) with buffer layers of strontium titanate ($SrTiO_3$, or STO) and lanthanum aluminate ($LaAlO_3$, or LAO), deposited by molecular beam epitaxy (MBE).[30,31]

Post-PLD fabrication steps are shown in Figure S1. After PLD deposition of YAP:Ce, the Si side of the imaging chip is polished using diamond lapping paper with 3, 1, and 0.5 μm grit (816−326, 816−328, and 816−330 from Ted Pella) followed by chemical mechanical planarization (CMP) polishing (Aptek Industries Inc.). After polishing, 1 μm of plasma-enhanced chemical vapor deposition (PECVD) silicon nitride is deposited on each side of the imaging chip (Oxford Plasmalab 80plus PECVD System at Marvell Nanofabrication Laboratory). Both sides are then photolithographically patterned using MICROPOSIT S1818 photoresist (Dow Chemical). The photoresist was spun onto the YAP:Ce chips at 2000 rpm (2000 rpm/s accelerating) resulting in a thickness of ∼0.8−1 μm. The chip was then placed on a hot plate at 110 °C for 1 min. After baking, the photolithography mask was placed on the chip, and it was exposed to UV light at 200 mW/cm^2 for 15 s (CS2010, Thorlabs). After UV exposure, the chip was developed in Microposit MF-319 Developer (Dow Chemical). Using these photolithography steps with different masks, an array of circles (each ∼10 μm across) was patterned on the YAP:Ce side of the chip and 4 × 4 array of ∼300 μm squares were patterned on the Si side of the chip using O_2/CF_4 reactive ion etching (RIE) (PETS Inc.) at 200 W with 40 sccm CF_4 and 10 sccm O_2 for ∼5 min or until the silicon nitride was entirely removed. The photoresist was then removed with Microposit S1818 Remover (Dow Chemical). To protect the YAP:Ce side of the chip during the tetramethylammonium hydroxide (TMAH) etch, ProTEK B3 Primer (Brewer Science) followed by ProTEK B3 (Brewer Science) were spin-coated on the YAP:Ce side of the chip. ProTEK B3 Primer was spin-coated at 2000 rpm (2000 rpm/s acceleration) and heated on a hot plate for 5 min at 220 °C. ProTEK B3 was then spin-coated at 2000 rpm (2000 rpm/s acceleration) and heated at 130 °C for 15 min and 220 °C for 40 min. As an additional layer of protection, a layer of polydimethylsiloxane (PDMS) (SYLGARD 184 Silicone Elastomer Kit, Dow Corning) was spin-coated on top of the ProTEK B3 layer at 1000 rpm (2000 rpm/s) and cured at 130 °C. The chip was then placed in an etch bath of 25% TMAH at 50 °C until the windows look transparent. After the etch, the ProTEK B3 and PDMS were removed with ProTEK Remover (Brewer Science).

PFO/F8BT Nanoparticle Preparation. Poly(9,9-di-*n*-octylfluorenyl-2,7-diyl) (PFO) and poly[((9,9-di-*n*-octylfluorenyl-2,7-diyl)-*alt*-co-(1,4-benzo-{2,1′,3}-thiadiazole)] (F8BT) were purchased from Solaris Chem Inc. To prepare PFO/F8BT nanoparticles, 20 μL of 50:50 1 wt % PFO and 1 wt % F8BT in *o*-xylene (Aldrich) were added to 100 μL of methanol while sonicating. Particle size is limited by filtration to 200 nm, but aggregation may occur after filtering. Particles were then quickly dropcast onto the CLAIRE imaging chip to prevent aggregation.

Deposition of Samples on CLAIRE Imaging Chips. 100 nm Ag nanocubes, 100 nm Ag nanoparticles coated with 20 nm SiO_2, and 50 nm Ag nanoparticles coated with 20 nm SiO_2 were purchased from NanoComposix. For imaging static samples, Ag nanoparticles and polymer nanoparticle were dropcast onto the CLAIRE imaging chip from an ethanol or methanol solution (Aldrich). For imaging Ag particles in ionic liquid, 100 nm Ag nanocubes were dropcast onto the CLAIRE imaging chip followed by 0.5 μL of 1-butyl-3-methylimidazolium hexafluorophosphate (BMIM PF_6, Aldrich). For imaging polymer nanoparticles in oil, a 100 μL solution of polymer nanoparticles in methanol was mixed with 100 μL of Edwards Ultragrade 19 (Edwards Vacuum). The methanol was then evaporated in a vacuum desiccator, and 0.5 μL was dropcast onto the CLAIRE imaging chip.

Secondary Electron and Cathodoluminescence Imaging. Cathodoluminescence (CL) and secondary electron (SE) images were acquired with a modified Zeiss Gemini SUPRA 55 Scanning Electron Microscope (SEM). An aluminum parabolic reflector was positioned above the same sample in order to couple a 1.3π sr solid angle of emission into a photomultiplier tube (Hamamatsu, H7421-40) outside of the vacuum chamber. All CLAIRE images were collected at 1.8 kV. The CL images of static Ag nanoparticles were acquired by averaging 20 frames at 2.56 s/frame with 512 × 512 pixel resolution. The CL images of static polymer nanoparticles were acquired as single frames at 25.6 s/frame with 512 × 512 pixels. CL movies of Ag nanoparticle desorption and polymer nanoparticle translation were collected at 2.56 s/frame.

CLAIRE Image Processing. All CLAIRE images were processed with ImageJ 1.48k and filtered with a Gaussian blur over 2−4 pixels (fwhm) to smooth over shot noise. CLAIRE images were either normalized to the maximum value of the data set (Figure 1) or to the background level (Figure 4).

Confocal Microscopy. Confocal microscopy images of PFO/F8BT nanoparticles were collected with an IX83 inverted microscope (Olympus) using a 20× 0.75 NA objective. All images were acquired with 512 × 512 and a scan rate of 10 ms/line using a 405 nm excitation source.

Photoluminescence and Absorption Spectra. Photoluminescence (PL) spectra of PFO/F8BT particles were collected with a Horiba Jobin Yvon Fluorolog-3 Spectrofluorimeter using an excitation wavelength of 405 nm. Absorption spectra of PFO/F8BT particles

DOI: 10.1021/acsnano.7b06081
ACS Nano 2017, 11, 10583−10590

were acquired with an Agilent Technologies Cary 100 UV−vis spectrophotometer.

CASINO Monte Carlo Simulations. Monte Carlo simulations of electron energy deposition were performed using the CASINO v3.2 program.[32] For each computation, 10000 electrons were simulated in a 1.2 nm $SrTiO_3$/ 20 nm $LaAlO_3$/15 or 20 nm $YAlO_3$ free-standing film. To determine the fraction of electrons penetrating through the film, the number of electrons penetrating through the film were divided by the 10000 simulated incident electrons. The energy deposition profile at 1.8 kV was generated by binning the energy deposition as a function of depth and then plotting the depth profile normalized to the total energy deposited.

Measuring Electron Penetration through YAP:Ce Free-Standing Films. To find an accelerating voltage appropriate for CLAIRE imaging with minimal electron penetration through the free-standing scintillator film, we measured the electron current through a free-standing $SrTiO_3/LaAlO_3$/YAP:Ce film for many different accelerating voltages. We divided the detected current by the incident current to determine the fraction of electrons that penetrate through the scintillator film. No current was detected below 2.0 kV.

Simulation of CLAIRE Images. Simulation of CLAIRE images was achieved by modeling the Ce^{3+} dopants in the scintillator film as a set of uncoupled transition dipole emitters located at different points in space. At each position, the electromagnetic response of a 100 nm Ag nanoparticle coated with a 20 nm SiO_2 shell and a 50 nm Ag nanoparticle coated with a 20 nm SiO_2 shell to the presence of a dipole emitter was calculated using the metallic nanoparticle boundary element method (MNPBEM) software package.[33] The resulting scattered electromagnetic field was then used to calculate the power radiated by the plasmon-dressed dipole emitter normalized to the power radiated by the dipole emitter in free space (P_0) using the following expresion[34]

$$\frac{P}{P_0} = 1 + \frac{6\pi\epsilon_0}{|\mu_0|^2}\frac{1}{k^3}\mathrm{Im}[\mu_0^* E_s(r_0)]$$

Here, μ_0 is the transition dipole moment of the emitter, ϵ_0 is the vacuum permittivity, and $E_s(r_0)$ is the emitter-induced scattered electric field of the plasmonic nanoparticle evaluated at the location of the emitter. The total power radiated by the plasmon-dressed emitter was calculated for dipole positions lying on a line, displaced 10 nm from the surface of the sphere along the z-axis, spanning from the center of the sphere radially outward to 300 nm. An orientational average in the xy plane for the emitter at each point in space along this line was performed, and the contribution of the plasmon-dressed emitter was recorded. The simulated scattered field $E_s(r)$ was also used to calculate the power radiated by the emitter-dressed plasmon,[35] and the total power radiated by the composite system (emitter plus plasmon) was calculated by summing the two. Maps were created from this line by utilizing the azimuthal symmetry of the sphere.

ASSOCIATED CONTENT

Supporting Information

The Supporting Information is available free of charge on the ACS Publications website at DOI: 10.1021/acsnano.7b06081.

Figures S1−S15 as noted in the text; supporting text on comparing the experimental and simulated CLAIRE images and comparing CLAIRE with other super-resolution imaging techniques (PDF)

CLAIRE imaging of Ag nanocube desorption from Figure 2B.(AVI)

Additional movie of Ag nanocube desorption (AVI)

AUTHOR INFORMATION

Corresponding Author

*E-mail: nsginsberg@berkeley.edu.

ORCID

Connor G. Bischak: 0000-0002-3071-4069

David J. Masiello: 0000-0002-1187-0920

Naomi S. Ginsberg: 0000-0002-5660-3586

Present Address

¶C.D.A.: Department of Bioengineering, Stanford University, Stanford, CA 94305, United States

Author Contributions

N.S.G. conceived of and supervised the project. C.G.B. and N.S.G. designed the research. C.G.B., R.B.W., C.L.H., and C.D.A. grew the YAP:Ce films and fabricated free-standing scintillator films. S.A. and D.F.O. advised on instrumentation and data acquisition software for CL imaging. C.G.B. performed CLAIRE imaging, analyzed CLAIRE image data, and performed CASINO simulations. Z.W. grew the Si/$SrTiO_3/LaAlO_3$ substrates. D.G.S. advised on $SrTiO_3/LaAlO_3$ film preparation. C.C., J.A.B., and S.C.Q. performed simulations to obtain simulated CLAIRE images. D.J.M. advised on the simulations. C.G.B. and N.S.G. wrote the manuscript, and all authors revised and approved the manuscript.

Notes

The authors declare no competing financial interest.

ACKNOWLEDGMENTS

YAP:Ce film deposition was supported by the National Science Foundation under Grant No. 1152656. Nanofabrication was supported by the Chemical Sciences, Geosciences and Biosciences Division, Office of Basic Energy Sciences, Office of Science, U.S. Department of Energy, FWP number SISGRN. Devices were fabricated both at the Marvell Nanofabrication Laboratory and Biomolecular Nanotechnology Center at UC Berkeley. CL at the LBL Molecular Foundry was performed as part of the Molecular Foundry user program, supported by the Office of Science, Office of Basic Energy Sciences, of the U.S. Department of Energy under Contract No. DE-AC02-05CH11231. The preparation of this manuscript was supported by STROBE, a National Science Foundation Science & Technology Center under Grant No. DMR 1548924. Z.W. and D.G.S. acknowledge support under AFOSR Grant No. FA9550-10-1-0123, C.G.B. and R.B.W. acknowledge an NSF Graduate Research Fellowship (DGE 1106400). D.J.M. acknowledges support from NSF CHE-1664684. N.S.G. acknowledges an Alfred P. Sloan Research Fellowship, a David and Lucile Packard Foundation Fellowship for Science and Engineering, and a Camille and Henry Dreyfus Teacher-Scholar Award. We thank E. K. Beutler for his input on the simulation results and L. W. Martin and R. Ramesh for access to PLD facilities.

REFERENCES

(1) Whitesides, G. M.; Grzybowski, B. Self-Assembly at All Scales. *Science* **2002**, *295*, 2418−2421.

(2) Zhang, S. Fabrication of Novel Biomaterials through Molecular Self-Assembly. *Nat. Biotechnol.* **2003**, *21*, 1171−1178.

(3) Williamson, M. J.; Tromp, R. M.; Vereecken, P. M.; Hull, R.; Ross, F. M. Dynamic Microscopy of Nanoscale Cluster Growth at the Solid−liquid Interface. *Nat. Mater.* **2003**, *2*, 532−536.

(4) Zheng, H.; Smith, R. K.; Jun, Y.; Kisielowski, C.; Dahmen, U.; Alivisatos, A. P. Observation of Single Colloidal Platinum Nanocrystal Growth Trajectories. *Science* **2009**, *324*, 1309−1312.

(5) Yuk, J. M.; Park, J.; Ercius, P.; Kim, K.; Hellebusch, D. J.; Crommie, M. F.; Lee, J. Y.; Zettl, A.; Alivisatos, A. P. High-Resolution

DOI: 10.1021/acsnano.7b06081
ACS Nano 2017, 11, 10583−10590

EM of Colloidal Nanocrystal Growth Using Graphene Liquid Cells. *Science* **2012**, *336*, 61−64.
(6) de Jonge, N.; Ross, F. M. Electron Microscopy of Specimens in Liquid. *Nat. Nanotechnol.* **2011**, *6*, 695−704.
(7) Ye, X.; Jones, M. R.; Frechette, L. B.; Chen, Q.; Powers, A. S.; Ercius, P.; Dunn, G.; Rotskoff, G. M.; Nguyen, S. C.; Adiga, V. P.; Zettl, A.; Rabani, E.; Geissler, P. L.; Alivisatos, A. P. Single-Particle Mapping of Nonequilibrium Nanocrystal Transformations. *Science* **2016**, *354*, 874−877.
(8) Kim, J.; Jones, M. R.; Ou, Z.; Chen, Q. *In Situ* Electron Microscopy Imaging and Quantitative Structural Modulation of Nanoparticle Superlattices. *ACS Nano* **2016**, *10*, 9801−9808.
(9) Betzig, E.; Patterson, G. H.; Sougrat, R.; Lindwasser, O. W.; Olenych, S.; Bonifacino, J. S.; Davidson, M. W.; Lippincott-Schwartz, J.; Hess, H. F. Imaging Intracellular Fluorescent Proteins at Nanometer Resolution. *Science* **2006**, *313*, 1642−1645.
(10) Hess, S. T.; Girirajan, T. P. K.; Mason, M. D. Ultra-High Resolution Imaging by Fluorescence Photoactivation Localization Microscopy. *Biophys. J.* **2006**, *91*, 4258−4272.
(11) Hell, S. W. Far-Field Optical Nanoscopy. *Science* **2007**, *316*, 1153−1158.
(12) Bates, M.; Huang, B.; Dempsey, G. T.; Zhuang, X. Multicolor Super-Resolution Imaging with Photo-Switchable Fluorescent Probes. *Science* **2007**, *317*, 1749−1753.
(13) Pavani, S. R. P.; Thompson, M. A.; Biteen, J. S.; Lord, S. J.; Liu, N.; Twieg, R. J.; Piestun, R.; Moerner, W. E. Three-Dimensional, Single-Molecule Fluorescence Imaging beyond the Diffraction Limit by Using a Double-Helix Point Spread Function. *Proc. Natl. Acad. Sci. U. S. A.* **2009**, *106*, 2995−2999.
(14) Yacobi, B. G.; Holt, D. B. *Cathodoluminescence Microscopy of Inorganic Solids*; Plenum Press: New York, 1990.
(15) Yamamoto, N.; Araya, K.; García de Abajo, F. J. Photon Emission from Silver Particles Induced by a High-Energy Electron Beam. *Phys. Rev. B: Condens. Matter Mater. Phys.* **2001**, *64*, 205419.
(16) Vesseur, E. J. R.; de Waele, R.; Kuttge, M.; Polman, A. Direct Observation of Plasmonic Modes in Au Nanowires Using High-Resolution Cathodoluminescence Spectroscopy. *Nano Lett.* **2007**, *7*, 2843−2846.
(17) Ropers, C.; Solli, D. R.; Schulz, C. P.; Lienau, C.; Elsaesser, T. Localized Multiphoton Emission of Femtosecond Electron Pulses from Metal Nanotips. *Phys. Rev. Lett.* **2007**, *98*, 043907.
(18) Kuttge, M.; Vesseur, E. J. R.; Koenderink, A. F.; Lezec, H. J.; Atwater, H. A.; García de Abajo, F. J.; Polman, A. Local Density of States, Spectrum, and Far-Field Interference of Surface Plasmon Polaritons Probed by Cathodoluminescence. *Phys. Rev. B: Condens. Matter Mater. Phys.* **2009**, *79*, 113405.
(19) Knight, M. W.; Liu, L.; Wang, Y.; Brown, L.; Mukherjee, S.; King, N. S.; Everitt, H. O.; Nordlander, P.; Halas, N. J. Aluminum Plasmonic Nanoantennas. *Nano Lett.* **2012**, *12*, 6000−6004.
(20) Myroshnychenko, V.; Nelayah, J.; Adamo, G.; Geuquet, N.; Rodríguez-Fernández, J.; Pastoriza-Santos, I.; MacDonald, K. F.; Henrard, L.; Liz-Marzán, L. M.; Zheludev, N. I.; Kociak, M.; García de Abajo, F. J. Plasmon Spectroscopy and Imaging of Individual Gold Nanodecahedra: A Combined Optical Microscopy, Cathodoluminescence, and Electron Energy-Loss Spectroscopy Study. *Nano Lett.* **2012**, *12*, 4172−4180.
(21) Atre, A. C.; Brenny, B. J. M.; Coenen, T.; García-Etxarri, A.; Polman, A.; Dionne, J. A. Nanoscale Optical Tomography with Cathodoluminescence Spectroscopy. *Nat. Nanotechnol.* **2015**, *10*, 429−436.
(22) Nawa, Y.; Inami, W.; Chiba, A.; Ono, A.; Miyakawa, A.; Kawata, Y.; Lin, S.; Terakawa, S. Dynamic and High-Resolution Live Cell Imaging by Direct Electron Beam Excitation. *Opt. Express* **2012**, *20*, 5629−5635.
(23) Glenn, D. R.; Zhang, H.; Kasthuri, N.; Schalek, R.; Lo, P. K.; Trifonov, A. S.; Park, H.; Lichtman, J. W.; Walsworth, R. L. Correlative Light and Electron Microscopy Using Cathodoluminescence from Nanoparticles with Distinguishable Colours. *Sci. Rep.* **2012**, *2*, 865.
(24) Willets, K. A.; Van Duyne, R. P. Localized Surface Plasmon Resonance Spectroscopy and Sensing. *Annu. Rev. Phys. Chem.* **2007**, *58*, 267−297.
(25) Jain, P. K.; Huang, X.; El-Sayed, I. H.; El-Sayed, M. A. Noble Metals on the Nanoscale: Optical and Photothermal Properties and Some Applications in Imaging, Sensing, Biology, and Medicine. *Acc. Chem. Res.* **2008**, *41*, 1578−1586.
(26) Novotny, L.; van Hulst, N. Antennas for Light. Nat. *Nat. Photonics* **2011**, *5*, 83−90.
(27) Kaz, D. M.; Bischak, C. G.; Hetherington, C. L.; Howard, H. H.; Marti, X.; Clarkson, J. D.; Adamo, C.; Schlom, D. G.; Ramesh, R.; Aloni, S.; Ogletree, D. F.; Ginsberg, N. S. Bright Cathodoluminescent Thin Films for Scanning Nano-Optical Excitation and Imaging. *ACS Nano* **2013**, *7*, 10397−10404.
(28) Bischak, C. G.; Hetherington, C. L.; Wang, Z.; Precht, J. T.; Kaz, D. M.; Schlom, D. G.; Ginsberg, N. S. Cathodoluminescence-Activated Nanoimaging: Noninvasive Near-Field Optical Microscopy in an Electron Microscope. *Nano Lett.* **2015**, *15*, 3383−3390.
(29) Anger, P.; Bharadwaj, P.; Novotny, L. Enhancement and Quenching of Single-Molecule Fluorescence. *Phys. Rev. Lett.* **2006**, *96*, 113002.
(30) Warusawithana, M. P.; Cen, C.; Sleasman, C. R.; Woicik, J. C.; Li, Y.; Kourkoutis, L. F.; Klug, J. A.; Li, H.; Ryan, P.; Wang, L.-P.; Bedzyk, M.; Muller, D. A.; Chen, L.-Q.; Levy, J.; Schlom, D. G. A Ferroelectric Oxide Made Directly on Silicon. *Science* **2009**, *324*, 367−370.
(31) Warusawithana, M. P.; Richter, C.; Mundy, J. A.; Roy, P.; Ludwig, J.; Paetel, S.; Heeg, T.; Pawlicki, A. A.; Kourkoutis, L. F.; Zheng, M.; Lee, M.; Mulcahy, B.; Zander, W.; Zhu, Y.; Schubert, J.; Eckstein, J. N.; Muller, D. A.; Hellberg, C. S.; Mannhart, J.; Schlom, D. G. $LaAlO_3$ Stoichiometry Is Key to Electron Liquid Formation at $LaAlO_3/SrTiO_3$ Interfaces. *Nat. Commun.* **2013**, *4*, 2351.
(32) Drouin, D.; Couture, A. R.; Joly, D.; Tastet, X.; Aimez, V.; Gauvin, R. CASINO V2.42—A Fast and Easy-to-Use Modeling Tool for Scanning Electron Microscopy and Microanalysis Users. *Scanning* **2007**, *29*, 92−101.
(33) Hohenester, U.; Trügler, A. MNPBEM − A Matlab Toolbox for the Simulation of Plasmonic Nanoparticles. *Comput. Phys. Commun.* **2012**, *183*, 370−381.
(34) Novotny, L.; Hecht, B. *Principles of Nano-Optics*; Cambridge University Press, 2006.
(35) Jackson, J. D. *Classical Electrodynamics*; Wiley, 1975.

DOI: 10.1021/acsnano.7b06081
ACS Nano 2017, 11, 10583−10590